Methacrylated Wood Flour-Reinforced Gelatin-Based Gel Polymer as Green Electrolytes for Li–O2 Batteries

Methacrylated wood flour-reinforced gelatin-based gel polymer as green electrolytes for Li-O_2 batteries

Mattia Longo[1], Carlotta Francia[1], Marco Sangermano[1], Minna Hakkarainen[2], Julia Amici[1*]

[1] Department of Applied Science and Technology, Politecnico di Torino, Corso Duca degli Abruzzi 24, 10129 – Torino, Italy

[2] KTH Royal Institute of Technology, Department of Fibre and Polymer Technology, Teknikringen 58, 100 44 Stockholm, Sweden

[*]Corresponding author: julia.amici@polito.it

Abstract

With its very high theoretical energy density, the Li-O_2 battery could be considered as a valid candidate for future advanced energy storage solutions. However, the challenges hindering the practical application of this technology are many, as for example electrolyte degradation under the action of superoxide radicals produced upon cycling. In that frame a new gel polymer electrolyte was developed starting from waste derived components: gelatine from cold water fish skin, waste from the fishing industry, and wood flour, waste from the wood industry. Both were methacrylated and then easily cross-linked through a one pot UV initiated free radical polymerization, directly in presence of the liquid electrolyte (0.5 M LiTFSI in DMSO). The wood flour works as cross-linking points reinforcing the mechanical properties of the obtained gel polymer electrolyte, but it also increases Li-ion transport properties with an ionic conductivity of 3.3 mS cm^{-1} and a transference number of 0.65 at room temperature. The Li-O_2 cells assembled with this green gel polymer electrolyte were able to perform 180 cycles at 0.1 mA cm^{-2}, at a fixed capacity of 0.2 mAh cm^{-2}, under constant O_2 flow. Cathodes *post-mortem* analysis confirmed that this new electrolyte was able to slow down solvent degradation, but it also revealed that the higher reversibility of the cells could be explained by

the formation of Li_2O_2 in the amorphous phase for a higher number of cycles compared to a purely gelatin-based electrolyte.

1. Introduction

In recent years, the heightened awareness towards environmental issues, such as the rise in average global temperatures due to extensive exploitation of fossil fuels, has led to a significant investment in renewable energy production technologies. Green and renewable energy sources (e.g. solar, wind and hydroelectric power) suffer from an intrinsic discontinuity, hindering their applicability and, thus, require powerful electrochemical storage devices in order to enable large scale implementation [1–4]. Since 1991, Li-ion-based storage devices have been widely considered and employed as the primary energy storage technology. However, they are now demonstrating their limitations in terms of energy density, which is practically about 260-300 Wh kg^{-1}, incapable of meeting the energy density requirements of electric or flying vehicles and smart grids [1,5,6]. Non-aqueous Li-air or Li-O_2 battery systems are interesting candidates for future high energy density applications, reaching an ultra-high theoretical energy density value of about 3500-3600 Wh kg^{-1}, comparable to that of gasoline, due to the $2\,Li + O_2 \rightleftharpoons Li_2O_2$ oxygen reduction reaction (ORR) at 2.96 V [7–11]. This incredibly high energy density can be mainly attributed to two factors: the absence of a cell-contained cathodic active material and the employment of Li metal as the anode [12]. Before these technologies can be scaled up in industry, several significant challenges need to be addressed. These include the short lifespan caused by clogging of the air cathode pores, the poor stability of the electrolytes in contact with lithium metal and the narrow operating temperature range [13–15]. One of the most pressing issues with Li-O_2 batteries is the poor safety stemming from the inherent flammability of the commonly used organic electrolytes. In the event of a short circuit, this flammability can lead to fire hazard. Additionally, evaporation and leakage of electrolytes, along with their degradation promoted by lithium metal and ORR intermediates, lead to capacity losses and,

ultimately, cell failure [16,17]. A possible solution to these critical problems is the deployment of a solid or semi-solid electrolyte system presenting excellent transference number, mechanical and thermal stability and limited permeability to O_2 and ORR intermediates. However, employing fully solid-state electrolytes, such as polymers or NASICON, garnet and perovskites, presents several additional challenges, namely lower ionic conductivity than liquid systems, low stability with Li metal and poor interfacial contact between electrodes and electrolyte which can increase cell polarization [16,18,19]. To address these problems, gel polymer electrolytes (GPE), consisting of a liquid phase immobilized in a polymeric matrix, have been widely employed. These systems offer clear operational advantages due to their balanced properties. They provide good mechanical and thermal stability, which enables the electrolyte to withstand dendrite-caused deformation, along with easy processability. Additionally, their excellent ionic conductivity enhances the efficiency and reversibility of galvanostatic cell cycling [20,21]. Numerous GPEs have been developed and characterized with various results. Wang et al. [22] developed a gel polymer electrolyte (GPE) consisting of poly(vinylidene fluoride-co hexafluoropropylene) (PVDF-HFP), trimethylolpropane ethoxylate triacrylate (TMPETA), and tetraglyme (T4) as a plasticizer. When combined with the integration of Ru nanoparticles into the air cathode, the cell exhibited superior cycling performance, lasting up to 2000 hours at 0.2 mA cm^{-2} at the curtailed capacity of 0.25 mAh cm^{-2}. Feng et al. demonstrated a PVDF-HFP based GPE containing 2,5-di-tert-butyl-1,4-benzoquinone (DBBQ, Aldrich) and N-methylphenothiazine (MPT) as redox mediators and N-methyl-N-propylpiperidinium bis(trifluoromethane sulfonyl)imide (PP13TFSI) ionic liquid as a plasticizer, capable of performing up to 100 cycles with a specific capacity of 1000 mAh g_C^{-1} at a current density of 100 mA g_C^{-1} [23]. However, in order to meet the environmental criteria of low carbon footprint in the development of new technologies, there is a push to reduce the usage of synthetic polymers in favour of biobased and eco-friendly alternatives such as

polysaccharides and cellulose. Song et al. employed a bacterial cellulose membrane, supporting a succinonitrile (SN) based GPE, which performed up to 40 cycles with a current density of 0.1 mA cm^{-2} at a limited specific capacity of 500 mAh g_C^{-1} [24]. In a previous work, our group demonstrated that gelatin can be easily methacrylated and crosslinked through UV mediated photopolymerization to obtain efficient GPEs. Gelatin, a biobased macromolecule derived by collagen (extracted by cold water fish skins) denaturation, possesses intriguing properties such as low cost and minimal environmental impact. Furthermore, it can directly react with methacrylic anhydride to form GelMA [25], a quite versatile oligomer sporting high biocompatibility, customizable photocrosslinkability and broadly tunable physico-chemical properties, enabling the creation of hydro and organo-gels for a wide variety of applications [25–28]. By employing waste materials, such as gelatin from the fish industry and wood flour from the wood industry, a more circular oriented approach to energy storage device manufacturing can be achieved, reducing the carbon footprint, and overall environmental impact, of batteries production. Here, a methacrylated wood flour (MWF) is synthesized [29] as reinforcement for the GPE production, which is developed following a previously reported protocol [30]. Its physico-chemical and electrochemical properties are compared to the bare GelMA based organogel. The reinforced membrane (GelMA10MWF20) displays excellent room temperature ionic conductivity of 3.33 mS cm^{-1} and high Li^+ transference number of 0.65. In the Li-O_2 cell, GelMA10MWF20 shows long lasting performance, reaching 60 cycles at a limited capacity of 0.5 mAh cm^{-2} and 180 cycles at a limited capacity of 0.2 mAh cm^{-2} with a current density of 0.1 mA cm^{-2}.

2. Experimental Section

2.1. Materials

Gelatine from cold water fish skin (Gel, average M_n= 60 kDa), methacrylic anhydride (MA, M_n= 154.16 g/mol), sodium hydroxide (NaOH, M_n= 40 g/mol), lithium bis(trifluoromethanesulfonyl)imide (LiTFSI, M_n= 287.1 g/mol), dimethyl sulfoxide (DMSO, M_n= 78.13 g/mol) and 2-hydroxy-1-(4-(2-hydroxyethoxy)phenyl)-2-methylpropan-1-one (Irgacure2959, M_n= 340.32 g/mol) were purchased from Sigma-Aldrich and used as received. Methacylated wood flour (MWF), synthesized as previously reported [29] and employed for GPE production without any further modifications.

2.2. GPE Production

The methacrylation of Gel was carried out following a protocol that was previously reported protocol [30]. Briefly, 10 g of Gel were solubilized in water at 50 °C under constant stirring. 6 g of MA were added dropwise and the solution was kept under stirring for 4 h with the addition of NaOH solution keeping the pH at 8. The obtained solution was dialyzed against distilled water and subsequently dried in an oven at 50 °C. The GelMA and MWF were further dried in a vacuum oven (Glass Oven B-585, Büchi, Uster, Switzerland) for 4 h at 40 °C before entering the glovebox (Mbraun Labstar, Stratham, NH, USA, O_2 and H_2O contents < 0.5 ppm) to avoid oxygen-induced radical polymerization inhibition. As for the previous characterization, 10% GelMA in the liquid electrolyte LiTFSI 0.5 M in DMSO was chosen as it showed the best compromise between mechanical and electrochemical properties [30]. 20% wt of MWF was added with respect to the GelMA weight and the solution was stirred on a hot plate until its complete dispersion. The photoinitiator Irgacure2959 was added to 2% with respect to the solid fraction weight. The obtained precursor solution was transferred on a glass sheet and irradiated with UV light (Hamamatsu UV LightningCure LC8 L9588, Hamamatsu, Shizuoka, Japan) for 5 minutes until completely cured. The obtained membranes were cut in disks of 18 mm diameter and with an average thickness of 300 μm.

2.3. Cell Assembly

Commercial gas diffusion layer disks (18 mm × 0.235 mm, GDL24BC, SIGRACET SGL Technologies, Meitingen, Germany) were used as cathodes after drying under vacuum for 6 h at 120 °C. The Li-O_2 test cells were assembled sandwiching the self-standing GelMA10 and GelMA10MWF20 membranes between the Li anode (15.6 mm × 0.62 mm, Chemetall s.r.l., Giussano, Italy) and the GDL24BC cathode in the Ar-filled glove box (MBraun Labstar, H_2O and O_2 content < 1 ppm) using an ECC-Air test cell (EL-Cell GmbH).

2.4. Physico-chemical Characterization

The polymerization process was examined by monitoring the presence of absorption peaks in the FT-IR spectra (Thermo Scientific Nicolet iS50 FTIR Spectrometer, Milan, Italy) obtained between 525 and 2000 cm^{-1} with 32 scans and a resolution of 4 cm^{-1}. The thermal stability of GelMA10 and GelMA10MWF20 was investigated by means of a thermogravimetrical analysis (TGA) with a Netzsch thermo-microbalance (TG 209 F3 Tarsus, Selb, Germany) in a N_2 atmosphere between 25 and 800°C with a temperature increase rate of 20 °C min^{-1}. Photorheometric analyses were conducted at room temperature to monitor the polymerization kinetics and the resulting storage moduli of the membranes. The time sweep tests were carried out with a parallel plate Anton PAAR Modular Compact Rheometer (Physica MCR 302, Graz, Austria) with quartz bottom glass and a gap value of 1 mm. A preliminar amplitude sweep test was carried out in order to evaluate the linear viscoelastic region (LVR) of the samples. All time sweep tests were conducted with an amplitude strain of 1 % and a frequency of 1 Hz. The UV irradiation was provided by Hamamatsu UV LightningCure LC8 L9588, turned on after 40 s. Mechanical compression tests were performed with MTS Systems Corporation dynamometer (MTS QTestTM/10 Elite, Eden Prairie, MN, USA) on cylindrical samples (diameter = 10 mm and average height = 3.5 mm) with a 10 N load cell and 1 mm min^{-1}

compression rate. The results were analyzed by TestWorks 4 software. All tests were conducted at room temperature. The morphological characterization of the membranes and the *post-mortem* analysis of the electrodes were investigated by means of a Field Emission Scanning Electron Microscope (FESEM, ZEISS Supra 40, Oberkochen, Germany). All measurements were performed in triplets.

2.5. Electrochemical Characterization

The ionic conductivity of the membranes was obtained by electrochemical impedance spectroscopy (EIS) performed with a VSP3-e multichannel potentiostat (Biologic, Seyssinet-Pariset, France) between 1 Hz and 10^5 Hz at open circuit voltage (OCV) with an amplitude of 0.01 V. The tests were carried out in the temperature range between 20 °C and 60 °C in a dynamic climatic chamber (BINDER GmbH, Tuttlingen, Germany) with a stainless-steel SS/GPE/SS cell configuration. The values of the ionic conductivities were computed by the equation:

$$\sigma = \frac{s}{(R_b \cdot A)} \qquad (1)$$

where s and A are the GPE thickness and contact area, respectively and R_b is the bulk resistance of the membranes obtained from the intercept of the high-frequency Nyquist plot of the EIS measurement. The Li-ion transference number (t_{Li^+}) of the GPEs were computed through EIS measurement before and after a chronoamperometry, carried out with a 10 mV voltage step over the OCV, performed on symmetrical Li/GPE/Li cells. The t_{Li^+} values were obtained through the Bruce-Vincent model with the following equation:

$$t_{Li^+} = \frac{I_s \cdot (\Delta V - I_0 R_0)}{I_0 \cdot (\Delta V - I_s R_s)} \qquad (2)$$

where I_s and I_0 are the steady state and initial currents, R_s and R_0 are the steady state and initial interfacial resistances and ΔV is the OCV perturbation (10 mV). The linear sweep voltammetry

(LSV) and the cyclic voltammetry (CV) analysis were carried out on Li/GPE/SS half cells and Li/GPE/GDL full cells respectively, in the voltage range between 2 V and 5 V with a 0.1 mV s^{-1} scan rate employing a CHI660D Electrochemical Workstation (CH Instruments, Inc, Austin, TX, USA). Plating and stripping tests were carried out by BT-2000 battery tester (Arbin Instruments, College Station, TX, USA) on symmetrical Li/GPE/Li cells with a current density of 0.1 mA cm^{-2} and a step time of 1 h. The full cells testing was performed on the BT-2000 battery tester with an O_2 flux of 4 ml min^{-1} between 2 V and 4.5 V with a current density of 0.1 mA cm^{-2}. The *post-mortem* XRD analysis on the GDLs of the tested cells was carried out by means of a high-resolution Philips X'Pert MPD powder diffractometer (Philips, Amsterdam, The Netherlands), between 10° and 90°, employing a Cu Kα radiation (V = 40 kV, I = 30 mA). All measurements were performed in triplets.

3. Results

3.1. Physico-chemical Characterization

The UV curing of the GelMA10 and GelMA10MWF20 membranes was investigated by means of FT-IR spectroscopy, monitoring the characteristic peaks of the methacrylic group during irradiation.

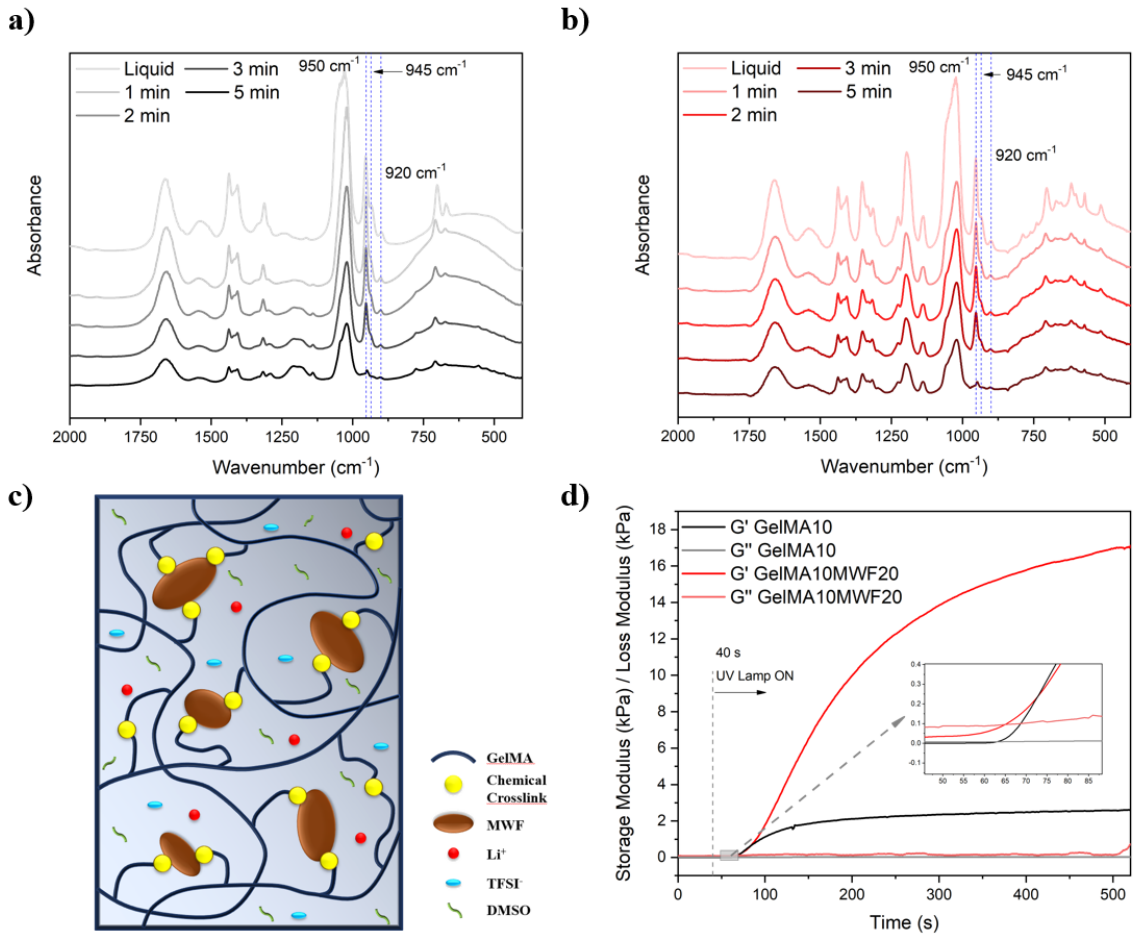

Figure 1. FTIR spectra after different irradiation times for a) GelMA10 and b) GelMA10MWF20. c) Schematic illustration of the crosslinked structure of GelMA10MWF20. d) Photorheometric curves of GPEs.

The GelMA10 spectrum, as well as the GelMA10MWF20 one, showed in Fig.1.a and b, present three intense bands at 1660 cm^{-1}, 1540 cm^{-1} and 1200 cm^{-1} (amide I, II and III, respectively) [31–33], completely covering the characteristic peak of the methacrylic group present at 1640 cm^{-1}. In the liquid precursor solution, before irradiation, three weak peaks are present at 920

cm^{-1}, 950 cm^{-1} and 945 cm^{-1}, associated with C-H stretching of C=C bonds (920 and 950 cm^{-1}) and $=CH_2$ wagging (945 cm^{-1}) [34–36], relative to the methacrylic moieties of the oligomers. The reduction in intensity of these peaks during the curing process is an indication of the C=C double bond reaction both from GelMA and MWF and therefore can be related to the successful polymerization, schematically reported in Fig.1.c. After confirming the correct polymerization of GelMA10 and GelMA10MWF20, the photoreactivity test was performed on the samples. This test involved monitoring the increase in the storage modulus of the formulations during UV irradiation. The UV lamp was turned on after 40 s from the start of the measurement, and the delay time needed for the crosslinking reaction to start is about 20 s for both samples. The crossover points between storage modulus (G') and loss modulus (G''), reported in Fig.1.d, is a description of the time needed to generate the gel network and occur at 23 s for the GelMA10 sample and at 25 s for the GelMA10MWF20. The slope of the storage modulus increase can be considered as an indication of the reaction kinetics [37]. In the initial phase, the slope of the curve is similar for both samples (Fig.S1). However, during the curing process the storage, modulus of the GelMA10 sample quickly reaches a plateau, supporting a final storage modulus of 2.6 kPa. In contrast, the GelMA10MWF20 sample has a much longer reaction time, due to the higher density of methacrylic groups, and reaches a final storage modulus of 17 kPa after 520 s. This substantial increase in the storage modulus is also mirrored in the enhanced mechanical properties. To validate the superior mechanical properties of the GelMA10MWF20 samples, a mechanical compression test was carried out. Fig.S2 shows the average stress-strain curves for the two formulations under investigation, from which the compression modulus was derived. The average value of the compression modulus for GelMA10MWF20 is 86.77 kPa, significantly higher than the 11.57 kPa observed for GelMA10, demonstrating the significative

effect of the MWF reinforcement. The superior mechanical properties of the reinforced GPE probably derive from the direct chemical crosslinking between the oligomer and the filler.

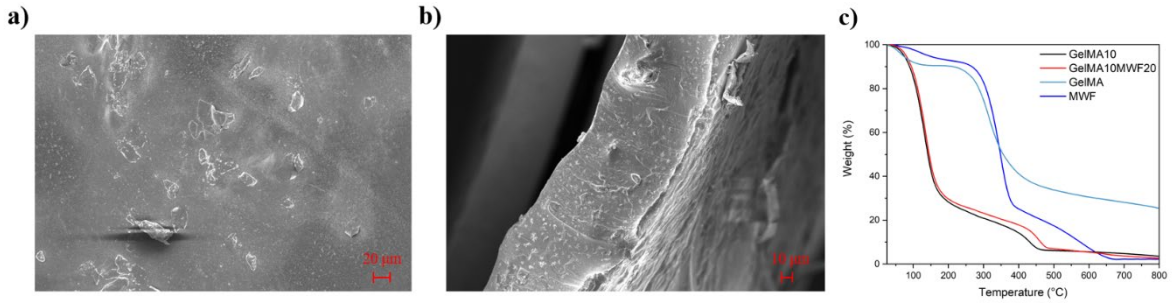

Figure 2. a) Surface and b) Cross-sectional SEM images of GelMA10MWF20 membrane. c) TGA curves of GelMA, MWF and GPEs.

A morphological analysis was carried out via SEM analysis on the GelMA10MWF20 to evaluate the dispersion of the MWF in the gel medium. In Fig.2.a, the absence of obvious porosities indicates the creation of a homogeneous gel phase capable of mitigating oxygen crossover between the electrodes. Fig.2.b clearly shows the good dispersion and excellent surface compatibility of the MWF particle, which are present both within the bulk of the membrane and on the surface. Lastly, the thermal stability of the UV-cured GelMA10 and GelMA10MWF20 samples was investigated by means of TGA, in order to evaluate their potential application in Li-O_2 systems. The thermogram (Fig.2.c and Fig.S3) of the MWF shows a first 8% weight reduction between 100 and 200 °C. This has been assigned to water evaporation, due to the water affinity of cellulose and lignin. The subsequent thermal degradation step can be associated to the degradation of hemicellulose first (with a maximum at 350 °C) and the decomposition of cellulose and lignin (between 480 and 680 °C) [29]. On the other hand, the UV-cured GelMA presents a 10% initial loss in weight due to water evaporation and a degradation step at about 200 °C, associated to the polymer chain bonds breaking, with a maximum at 318 °C. The thermograms of both photocured membranes present

a first weight reduction step between 50 and 200 °C, probably due to evaporation of water traces followed by evaporation of DMSO (T_{eb} = 189 °C), with an onset temperature of 57.4 and 62.4 °C, respectively for GelMA10 and GelMA10MWF20. The second degradation step is associated to the GelMA thermal degradation and occurs between 400 and 500 °C with a maximum at 430 and 454 °C respectively for GelMA10 and GelMA10MWF20. No distinct degradation step associated with MWF is evident in the TGA profile of GelMA10MWF20. However, a slight increase in the thermal stability is observed for GelMA10MWF20, stemming from the higher thermal stability of MWF with respect to the crosslinked GelMA [29,36,38]. Additionally, the involvment of MWF in the formation of a cross-linked network through the reaction of the methacrylic moieties contributes to this effect [29].

3.2. Electrochemical Characterization

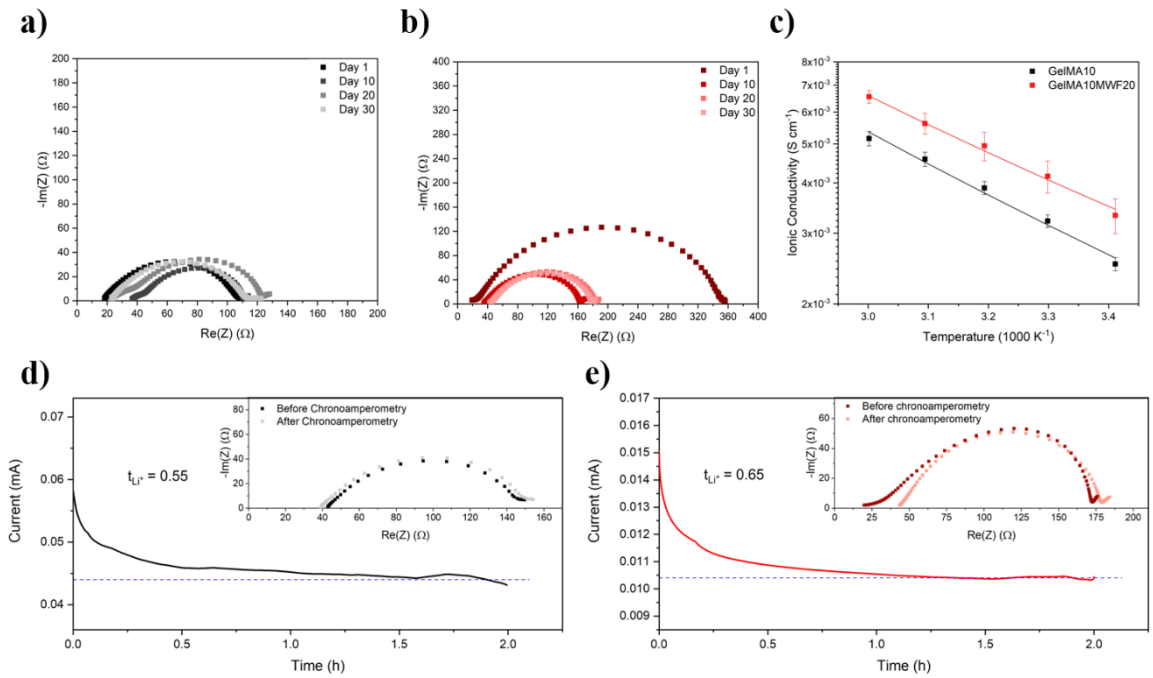

Figure 3. Time evolution of impedance spectra of a symmetric Li/Li cell containing a) GelMA10 and b) GelA10MWF20. c) Temperature dependence of ionic conductivity of GPEs. Chronoamperometry curves of symmetric Li/Li cells containing d) GelMA10 and e)

GelMA10MWF20. Inserts: Impedance spectra of Li/Li cells before and after the chronoamperometry.

To evaluate the interfacial stability of the biobased GPE membrane with metallic lithium, EIS measurements were conducted daily for a month on symmetrical Li/GPE/Li cells at OCV. The resulting Nyquist plots are shown in Fig. 3.a and 3.b. The interfacial resistance R_{ct} of the GelMA10MWF20 sample, compared to the bare GelMA10 membrane, shows a slight change with the addition of the MWF particles. The pristine GelMA10MWF20 containing cell reaches a value of R_{ct} of 340 Ω, against the 100 Ω of the pristine GelMA10 one. This significant increase in interfacial resistance can be ascribed to the presence of a solid non-conductive fraction dispersed in the gel medium, which increases the rigidity of the membrane and initially worsens the interfacial contact during the first day. However, after 10 days, the R_{ct} decreases to about 120 Ω, demonstrating the formation of an interfacial layer able to improve the contact between lithium surface and membrane. The stability of such layer, in contact with lithium metal, is confirmed by the small variation of R_{ct} after one month, resulting in a fluctuation of about ±20 Ω. The bulk resistance R_b, corresponding to the intercept of the high frequency region of the Nyquist plot, does shows no significative difference between the GelMA10 and GelMA10MWF20, remaining almost constant at 20 and 40 Ω, respectively, through the observed time window. This suggests that the formulation is inherently stable when in contact with lithium metal and, thereby confirming the applicability of these membranes in Li-O_2 batteries applications. The ionic conductivity of the electrolyte is another key parameter for solid state Li-O_2 batteries applications. The ionic conductivity was evaluated with Equation 1, where the R_b term was obtained by EIS measurements performed on symmetrical SS/GPE/SS cells in the temperature range between 20 °C and 60 °C. Both samples follow a linear trend with a clear Arrhenius-like behaviour (Fig.3.c) which is due to the diffusion-based conduction

mechanism [39]. The obtained ionic conductivity values for GelMA10 are 2.51 mS cm^{-1} at 20 °C and 5.16 mS cm^{-1} at 60 °C, while GelMA10MWF20 reaches an excellent 3.33 mS cm^{-1} at 20 °C and 6.57 mS cm^{-1} at 60 °C, resulting in an ionic conductivity comparable with liquid electrolyte systems [39–41]. The excellent ionic conductivity displayed by the GelMA10MWF20 membrane stems from the probable reduction in crystallinity, which increase the segmental motion of the polymer chains [42]. Another possible effect of the addition of MWF particles is the joint interaction between the polar groups (C=O) on the surface of the particles as well as on the GelMA chains, increasing the Li salt dissociation and creating preferential conduction channels around the external surfaces of the filler dispersed in the bulk of the membrane [43]. These "conduction highways" could reduce significatively the resistance that the membrane opposes to the ionic movement, thus incrementing ionic mobility [44]. The transference number t_{Li^+} was evaluated by means of two EIS measures before and after the chronoamperometry on a symmetrical Li/GPE/Li cell with a voltage step of 10 mV over the OCV. The t_{Li^+} of the GPE gives an indication on the ratio of current transported by Li^+ ions. An increase of t_{Li^+} is directly linked to the reduction of ionic gradients in the electrolyte resulting in limited concentration polarization. Furthermore, the increase of t_{Li^+} leads to homogeneous lithium deposition on the electrode surface and the inhibition of dendritic growth [45]. The GelMA10 membrane displays a t_{Li^+} of 0.55, while the GelMA10MWF20 one reaches 0.65 (Fig.3.d and e). This increase in the transference number and, consequently in the Li^+ mobility, can be directly linked to the generation of preferential Li^+ conduction channels on the surface of the filler particles, as well as the inhibition of the $TFSI^-$ anions migration via interaction with the Lewis acid sites present on the surface of the MWF particles [46–49]. Another fundamental property of the electrolyte in the Li-O_2 battery is the electrochemical stability in contact with metallic lithium under operating potential. To evaluate the electrochemical stability window (ESW) a LSV analysis was carried out on a half

Li/GPE/SS cell in the potential range between 2 V and 5 V at room temperature and the results are reported in Fig.4.a.

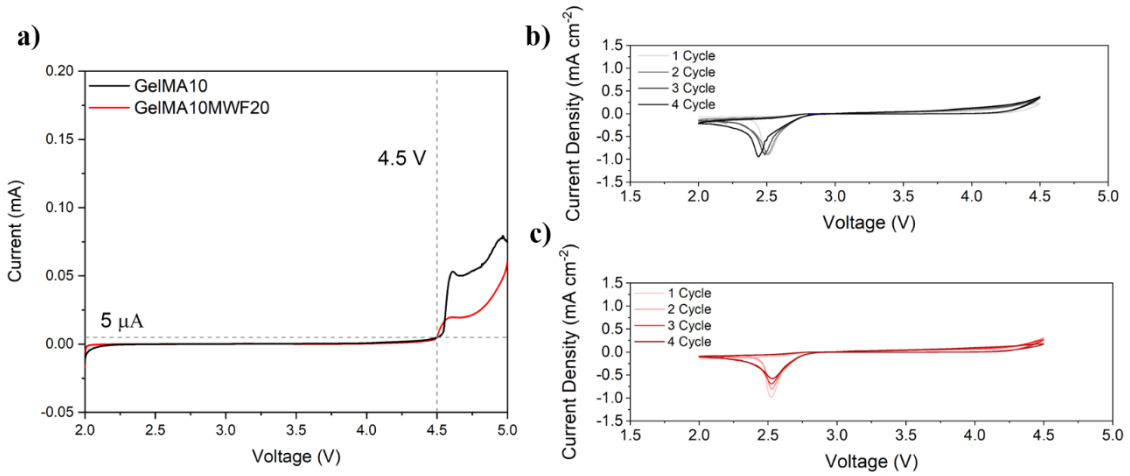

Figure 4. a) LSV curves of Li/SS half cells. CV curves of Li/GDL full cells containing b) GelMA10 and c) GelMA10MWF20.

The GelMA10MWF20 sample shows a comparable electrochemical stability window in the anodic branch with respect to the GelMA10 membrane, both demonstrating no electrolyte degradation reactions until 4.5 V, considering a current threshold value of 5 µA, and thus, resulting electrochemically stable in the operational potential range. The cyclic voltammetry (CV) analysis was carried out on full cells (Li/GPE/GDL24BC) in cycling conditions (4 ml min^{-1} O_2 flow), in order to evaluate the evolution of the electrochemical reactions during cycling. The voltammograms reported in Fig.4.b and c show the clear peak of the cathodic ORR reaction occurring at 2.52 V for both GelMA10 and GelMA10MWF20. After 4 cycles, the GelMA10MWF20 cell displays no shift in the peak maximum, as opposed to the maximum of the GelMA10 containing cell, which decreases to 2.44 V.

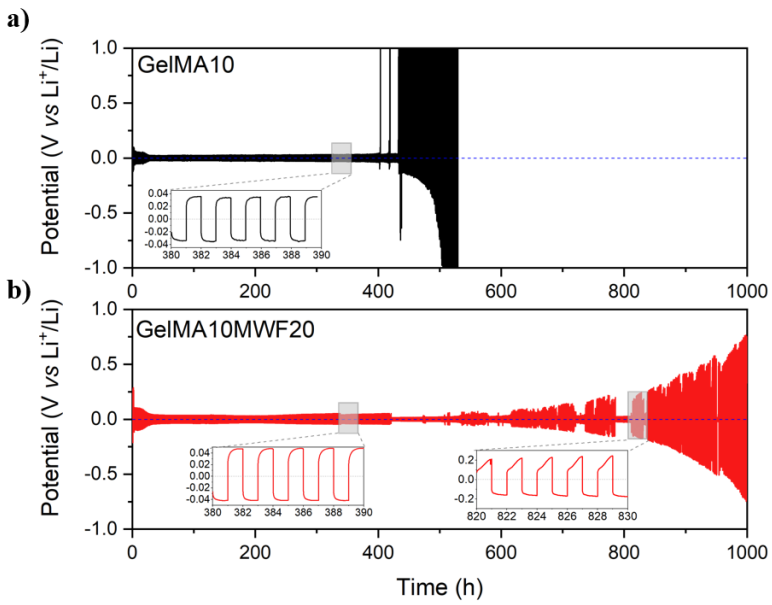

Figure 5. a) GelMa10 and b) GelMA10MWF20 galvanostatic Li plating and stripping profiles of symmetric Li/Li cells at a current density of 0.1 mA cm^{-2} and a limited capacity of 0.1 mAh cm^{-2}.

The ORR onset potential for the GelMA10 cell in the first CV cycle is 2.89 V, while is 2.86 V for the GelMA10MWF20. The GelMA10MWF20, however, demonstrates limited cell polarization, retaining an ORR onset potential (Fig.S4) of 2.85 V at the fourth cycle, as opposed to the 2.84 V displayed by the GelMA10 cell [50]. The lower cell polarization displayed by the reinforced membrane is consistent with the higher ionic conductivity and superior transport properties of such GPEs. The increase in the area of the cathodic peak after the first cycle in the GelMA10 and after the second cycle in the GelMA10MWF20 can be associated with a slower kinetics of the ORR due to the onset of nucleation of crystalline discharge products [51]. To further probe the GPEs transport properties and the electrochemical stability during cycling, Li/GPE/Li symmetrical cells were also assembled and tested under a current density of 0.1 mA cm^{-2} with a step time limit of 1 h (limited capacity of 0.1 mAh cm^{-2}) at room temperature.

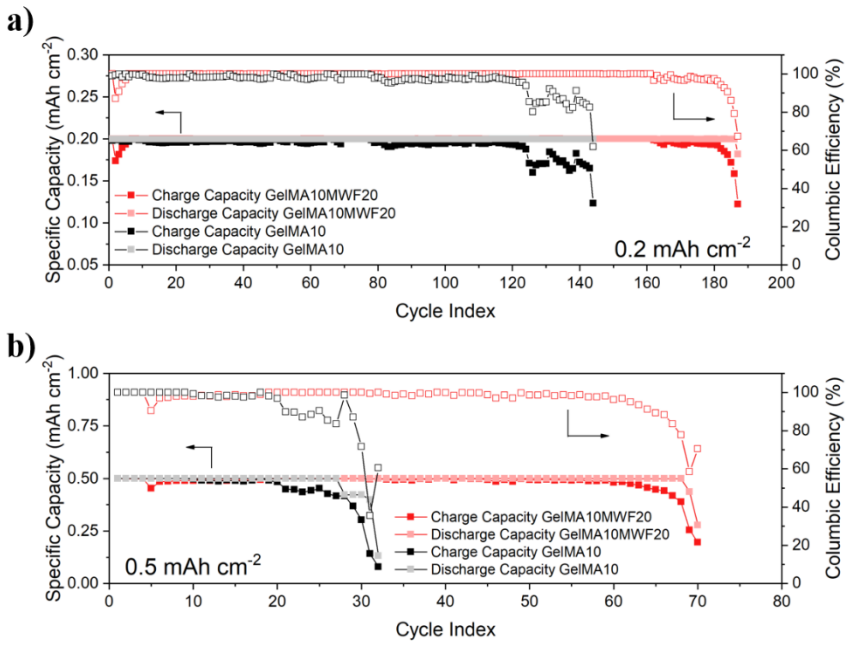

Figure 6. Charge/discharge capacities and columbic efficiency for Li/GDL full cells containing a) GelMA10 and b) GelMA10MWF20. All tests were carried out with a current density of 0.1 mA cm^{-2}.

As shown in Fig.5.a and b, both cells are able to cycle for 400 h, sporting a low overpotential of 36 mV and 47.8 mV for GelMA10 and GelMA10MWF20, respectively. A slightly higher overpotential is recorded for the reinforced membrane, likely due to poorer interfacial contact resulting from its superior mechanical properties. Nonetheless, the long cycling life and the stable and flat voltage profile for each cycle demonstrate the good compatibility of both GPEs with Li metal as well as the low energy barrier towards Li^+ dissolution and deposition and the limited production of dead lithium [44]. The GelMA10 cell exhibits significant dendritic growth, evidenced by potential spikes, followed by an increase in potential up to 5 V due to cell polarization. The reinforced membrane, on the other hand, presents limited dendritic growth resulting in micro-short circuits, which cause a decrease in the overpotential [52,53]. This limited dendritic growth, however, does not result in the catastrophic death of the cell, but

the GelMA10MWF20 containing cell is able to continue cycling with a low enough overpotential up until 1000 h of operation, possibly due to the long-term superior mechanical stability due to the MWF addition. After 800 cycles the voltage profile is still reasonably flat, although higher, for one GPE/Li interface, while presents a sharper increase for the other interface, caused by dendritic growth and accumulation of dead Li. Li/GPE/GDL24BC full cells were assembled to further probe the electrochemical properties of the reinforced membrane as well as to assess the stability of the electrolyte during operation. Fig.S5 display the full galvanostatic discharge curves for both GelMA10 and GelMA10MWF20 when cycled at different current densities. Both cells present similar voltage profile during discharge at each current density from 0.05 mA cm^{-2} up to 1 mA cm^{-2}, reaching values up to around 9 mAh cm^{-2} at 0.05 mA cm^{-2} and 5.55 mAh cm^{-2} at 1 mA cm^{-2}, with a reasonably flat discharge voltage plateau. The linear trend of the specific discharge capacity is reported in Fig.S6, with the obtained values of discharge capacity comparable to those reported in other studies [9,18–20,22,47]. Li/GPE/GDL24BC full cells were galvanostatically cycled with a limited capacity of 0.2 mAh cm^{-2} and a current density of 0.1 mA cm^{-2}, in order to assess their stability in operation. The resulting voltage profiles and specific capacity retention are reported in Fig.6.a and b and Fig.S7.a and b. The GelMA10 reference cell presents stable cycling with reversible charge and discharge voltage profiles up until 120 cycles of operation (corresponding to a lifetime of 480 h), good capacity retention and Columbic efficiency of 98.18 ± 0.1%. After the first 120 cycles, the GelMA10 cell is still able to cycle up to 140 cycles with lower Columbic efficiency of 86.27 ± 1.4%. In contrast, the GelMA10MWF20 cell displays a longer lifetime and stability, reaching 160 cycles with excellent capacity retention and a Columbic efficiency of 99.98 ± 0.01%. After 160 cycles, the GelMA10MWF20 continues to cycle reversibly until 187 cycles with Columbic efficiency of 94.8 ± 1.32% before experiencing a significative drop in charge capacity (Fig.6.a). This is probably due to degradation of cell components and the

accumulation of irreversible products in the cathode porosities. The overpotential of the cells is another indicator of the reversibility of the galvanostatic cycling and was computed considering the difference between the charge and discharge voltage values at a capacity of 0.1 mAh cm^{-2}. Fig.S7.c shows a stable overpotential for both GPEs, with a higher average overpotential value of 1.41 V retained for 100 cycles for GelMA10 with respect to 1.36 V for GelMA10MWF20 after 180 cycles. Comparing this result with the higher overpotential demonstrated by the GelMA10MWF20 in the Li/GPE/Li galvanostatic cycling test, it can be concluded that the higher rigidity, and therefore higher interfacial resistance displayed by the reinforced membrane is largely compensated after a few cycles in an O_2 atmosphere, by a slowing down of the degradation processes. The higher cycling stability and longer operational lifetime of the GelMA10MWF20 cells with respect to the GelMA10 one can be, thus, attributed to the significative increase in the mechanical stability, as well as in the crosslinking density, due to the presence of the MWF particles dispersed in the gel medium [20]. Another possible indication of the stability of the cycling is the terminal voltage values for each cycling step, reported in Fig.S7.d. Both considered samples display a similar behaviour with almost constant values of terminal discharge potential. Specifically, GelMA10MWF20 shows a terminal discharge voltage of 2.77 V after 160 cycles, while GelMA10 maintains a voltage of 2.75 V for the first 100 cycles. The GelMA10 cell displays a slower and more gradual drop in the terminal discharge potential reaching 2.5 V after 120 cycles and 2 V after 144 cycles, while the GelMA10MWF20 cell experience a sharper drop from 2.7 V after 175 cycles to 2 V after 186 cycles. Considering the superior mechanical and electrochemical stability of the reinforced GPEs, another galvanostatic cycling test was conducted with a higher limited capacity. Fig.6.b and Fig.S8.a and b show the trend of capacity retention for GelMA10 and GelMA10MWF20 cells, cycled with a current density of 0.1 mA cm^{-2} and a limited capacity of 0.5 mAh cm^{-2}. The GelMA10MWF20 cell presents a longer lifetime than the GelMA10 one, reaching up to 60

cycles (corresponding to a life span of 600 h of operation) with an average Columbic efficiency of 98.84 ± 0.19%, demonstrating a significative improvement with respect to GelMA10, which reached 20 cycles with a Columbic efficiency of 99.01± 0.23%. Nonetheless, the GelMA10MWF20 was able to continue cycling up to 70 cycles, with a lower efficiency of 85.57 ± 3.5%, demonstrating a cycle life twice as long as the one without reinforcement (Fig.6.b). The voltage profiles of both cells are stable and demonstrate the excellent reversibility of the galvanostatic cycling in the test conditions, with the GelMA10MWF20 cell presenting a stable charge/discharge behaviour until the 60th cycle. The overpotential of the cells cycling at 0.5 mAh cm^{-2} was computed considering the charge and discharge potentials at a capacity of 0.25 mAh cm^{-2}, and its evolution is reported in Fig.S8.c. Both cells exhibit minimal polarization as evidenced by the low average value of the computed overpotential, reaching 1.35 V in the 20 cycles for GelMA10 and 1.27 V in the 60 cycles for the GelMA10MWF20 cell. The decrease in the overpotential during the first 20 cycles has been associated to the decrease in the degradation of DMSO and therefore a limited deposition of degradation products on the electrodes surface in the first cycles. The improved stability of the GelMA10MWF20 formulation can be attested considering the stable terminal discharge potential of 2.77 V until 40 cycles, decreasing to 2.5 V after 60 cycles and to 2 V after 70 cycles (Fig.S8.d).

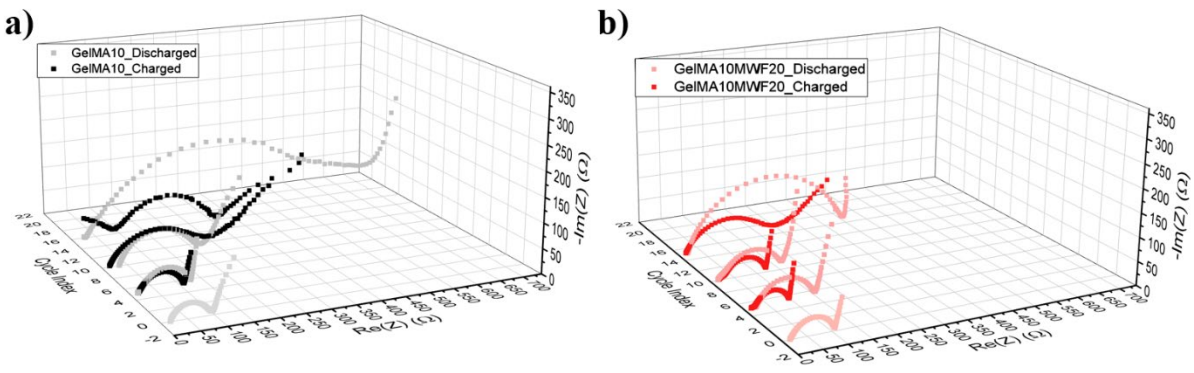

Figure 7. Impedance spectra evolution of Li/Li cells after 5, 10 and 20 galvanostatic charges and discharges with a current density of 0.1 mA cm^{-2} and a limited capacity of 0.5 mAh cm^{-2} for a) GelMA10 and b) GelMA10MWF20.

For the GelMA10 cell the terminal discharge potential has a sharper drop after 20 cycles, reaching 2 V after 32 cycles. For both cells, the terminal charge potential remains constant at around 4.5 V for the entire operational life in both cycling tests. To better characterize the charge and discharge products XRD and EIS measurements were carried out on full Li/GPE/GDL24BC cells containing GelMA10 and GelMA10MWF20, after 5, 10 and 20 cycles of galvanostatic charge and discharge. The cells were cycled with a current density of 0.1 mA cm^{-2} and a fixed areal capacity of 0.5 mAh cm^{-2}, starting after a rest time of 6 h in a pure O_2 atmosphere. The results of the EIS measurements were analysed by means of ZView software and the values of resistances, as well as the equivalent circuit are reported in Fig.7.a and b, Fig.S9 and in Tab.S1. It is clear to see that the R_{ct} associated to the fresh cells depends on the modulus of the GPE, so that the GelMA10 membrane presents a lower value of charge-transfer resistance compared to the reinforced GPE, in accordance with what was initially observed (lithium plating and stripping, interfacial stability). The benefit of the reinforcement effect due to the MWF presence becomes clear considering the limited increase of R_{ct} upon cycling, with the GelMA10 cell reaching a R_{ct} of 427.11 Ω after 20 cycles, as opposed to the 338.4 Ω of the GelMA10MWF20 cell. Moreover, the superior reversibility of the electrochemical reactions in the GelMA10MWF20 cell is demonstrated by the higher difference between the R_{ct} values after discharge and charge, indicating the presence of more reversible discharge products deposited in the GDL porosities. After the 20^{th} recharge, the reinforced membrane displays a R_{ct} of 168.7 Ω while the GelMA10 cell shows a charge-transfer resistance of 193.7 Ω, confirming the presence of insulant and irreversible discharge products in the GDL porosities.

The XRD diffractograms reported in Fig.S10.a and b demonstrate the generation of mainly amorphous Li_2O_2 after the first 10 cycles, associated with the absence of the characteristic Li_2O_2 peaks at 32° and 35° [54–56]. The increase in R_{ct} by EIS can be linked to the deposition during discharge of crystalline Li_2O_2 during discharge, confirmed by the appearance of the peaks at 32° and 35° in the GelMA10 discharge XRD spectrum for the 20th discharge. As for the GelMA10MWF20 cell, the cycled GDL does not present the crystalline Li_2O_2 peaks, suggesting a continued amorphous deposition of the discharge products. The deposition of discharge products with different crystalline structure (crystalline and amorphous Li_2O_2) is confirmed by the presence in the voltage profiles of the cells of two different discharge plateau. The more significative one, at 2.78 V, refers to the deposition of amorphous Li_2O_2 via the "surface-mediated" reaction mechanism, while the one found at 3.15 V refers to the deposition of crystalline products via the "solution-mediated" mechanism. During the first cycles, non-crystalline Li_2O_2 is the main deposited specie during discharge. Such film-like amorphous discharge products are reported to theoretically display higher transport properties and are mainly associated with the "surface-mediated" reaction mechanism [57,58]. This mechanism should be theoretically displayed in low-donor number (DN) solvents, but its occurrence in high-DN such as DMSO, has been reported in literature [59,60] and it is further confirmed by the presence of a distinct plateau in the charging voltage profile (at around 3.8 V) and a longer initial sloping region, both associated with the decomposition of amorphous Li_2O_2 [7]. With the increase in the number of cycles and the degradation of the electrolyte, the voltage plateau associated with the deposition of crystalline Li_2O_2 become more significative, and thus a crystalline core is probably first deposited, followed by the amorphous Li_2O_2 deposition. Such crystalline cores are decomposed at higher potentials with respect to the amorphous one during the charge process and thus can be retained as un-decomposed discharge products in the cathode porosities, increasing the R_{ct} of the cell. The absence of clear crystalline discharge

products in the GDL recovered from the cycled GelMA10MWF20 cell is confirmed by the SEM micrograms reported in Fig.S11.b and c, where the morphology of the GelMA10MWF20 GDL is similar to the pristine GDL morphology (Fig.S11.a). Due to the lower mechanical properties and the superior infiltration of the GelMA10 in the cathode porosities, the disassembly of the cell was considerably more difficult. The reported microgram refers to the cathode exposed from a crack in the GPE and present a significantly more passivated GDL with the presence of larger discharge products. Such different behaviour in the evolution of the cathodic reactions, arise from the improved electrochemical and transport properties of the reinforced GPE, as well as from a superior protection of the Li metal anode surface [61].

4. Conclusions

In this work, methacrylated wood flour (MWF) was employed as a mechanical reinforcement in a methacrylated gelatin (GelMA) based gel polymer electrolyte, implemented in a Li-O_2 battery system. The reinforced GPEs present superior mechanical and lithium transport properties, associated with the presence of the passive filler, reaching a room temperature ionic conductivity of 3.33 mS cm^{-1} and presenting a superior transference number of 0.65. Tested full cells display an improved cycle stability reaching 180 cycles at 0.1 mA cm^{-2} and a limited capacity of 0.2 mAh cm^{-2} and 60 cycles with a limited capacity of 0.5 mAh cm^{-2}. The reinforced membrane shows higher interfacial resistance, caused by the superior stiffness. However, this effect is fully compensated by a decrease in the degradation of the liquid electrolyte. The superior electrochemical stability of GelMA10MWF20 and the longer operational lifetime are theorized to stem from the deposition of highly reversible, amorphous discharge products in the GDL porosities, credited to increase the lifetime of the cell due to their superior transport properties. Such hypothesis is confirmed by the absence of the crystalline discharge products peaks in the diffractograms of the *post-mortem* GDL, as well as the presence of different voltage plateau in the charge and discharge profiles of the cycling cells, referring to the Li_2O_2

deposition via two different reaction mechanisms. In conclusion, the composite GelMA10MWF20 GPE, reinforced with MWF, exhibits superior properties compared to the non-reinforced membrane. This represents a clear optimization towards increasingly high-performance gel polymer electrolytes obtained from waste materials such as gelatin and wood flour. It can be considered an intriguing candidate for future, greener Li-O_2 battery applications.

Bibliography

[1] Z. Zhu, T. Jiang, M. Ali, Y. Meng, Y. Jin, Y. Cui, W. Chen, Rechargeable Batteries for Grid Scale Energy Storage, Chem Rev 122 (2022) 16610–16751. https://doi.org/10.1021/acs.chemrev.2c00289.

[2] Z. Wu, Y. Tian, H. Chen, L. Wang, S. Qian, T. Wu, S. Zhang, J. Lu, Evolving aprotic Li-air batteries, Chem Soc Rev 51 (2022) 8045–8101. https://doi.org/10.1039/d2cs00003b.

[3] C. Dang, Q. Mu, X. Xie, X. Sun, X. Yang, Y. Zhang, S. Maganti, M. Huang, Q. Jiang, I. Seok, W. Du, C. Hou, Recent progress in cathode catalyst for nonaqueous lithium oxygen batteries: a review, Adv Compos Hybrid Mater 5 (2022) 606–626. https://doi.org/10.1007/s42114-022-00500-8.

[4] P.U. Nzereogu, A.D. Omah, F.I. Ezema, E.I. Iwuoha, A.C. Nwanya, Anode materials for lithium-ion batteries: A review, Applied Surface Science Advances 9 (2022). https://doi.org/10.1016/j.apsadv.2022.100233.

[5] Y. Chen, J. Xu, P. He, Y. Qiao, S. Guo, H. Yang, H. Zhou, Metal-air batteries: progress and perspective, Sci Bull (Beijing) 67 (2022) 2449–2486. https://doi.org/10.1016/j.scib.2022.11.027.

[6] S. Matsuda, M. Ono, S. Yamaguchi, K. Uosaki, Criteria for evaluating lithium-air batteries in academia to correctly predict their practical performance in industry, Mater Horiz 9 (2022) 856–863. https://doi.org/10.1039/d1mh01546j.

[7] T. Liu, J.P. Vivek, E.W. Zhao, J. Lei, N. Garcia-Araez, C.P. Grey, Current Challenges and Routes Forward for Nonaqueous Lithium-Air Batteries, Chem Rev 120 (2020) 6558–6625. https://doi.org/10.1021/acs.chemrev.9b00545.

[8] K. Chen, D.Y. Yang, G. Huang, X.B. Zhang, Lithium-Air Batteries: Air-Electrochemistry and Anode Stabilization, Acc Chem Res 54 (2021) 632–641. https://doi.org/10.1021/acs.accounts.0c00772.

[9] J. Lei, Z. Gao, L. Tang, L. Zhong, J. Li, Y. Zhang, T. Liu, Coupling Water-Proof Li Anodes with LiOH-Based Cathodes Enables Highly Rechargeable Lithium–Air Batteries Operating in Ambient Air, Advanced Science 9 (2022). https://doi.org/10.1002/advs.202103760.

[10] J. Lai, Y. Xing, N. Chen, L. Li, F. Wu, R. Chen, Electrolytes for Rechargeable Lithium–Air Batteries, Angewandte Chemie - International Edition 59 (2020) 2974–2997. https://doi.org/10.1002/anie.201903459.

[11] H.-F. Wang, X.-X. Wang, F. Li, J.-J. Xu, Fundamental Understanding and Construction of Solid-State Li−Air Batteries, Small Science 2 (2022) 2200005. https://doi.org/10.1002/smsc.202200005.

[12] Y. Shao, F. Ding, J. Xiao, J. Zhang, W. Xu, S. Park, J.G. Zhang, Y. Wang, J. Liu, Making Li-air batteries rechargeable: Material challenges, Adv Funct Mater 23 (2013) 987–1004. https://doi.org/10.1002/adfm.201200688.

[13] G. Huang, J. Wang, X. Zhang, Electrode Protection in High-Efficiency Li-O2Batteries, ACS Cent Sci 6 (2020) 2136–2148. https://doi.org/10.1021/acscentsci.0c01069.

[14] J. Wang, Y. Li, X. Sun, Challenges and opportunities of nanostructured materials for aprotic rechargeable lithium-air batteries, Nano Energy 2 (2013) 443–467. https://doi.org/10.1016/j.nanoen.2012.11.014.

[15] C. Wang, Z. Guo, S. Zhang, G. Chen, S. Dong, G. Cui, Constructing in-situ polymerized electrolyte on lithiophilic anode for high-performance lithium–air batteries operating in ambient conditions, Energy Storage Mater 43 (2021) 221–228. https://doi.org/10.1016/j.ensm.2021.08.041.

[16] X. Chi, M. Li, J. Di, P. Bai, L. Song, X. Wang, F. Li, S. Liang, J. Xu, J. Yu, A highly stable and flexible zeolite electrolyte solid-state Li–air battery, Nature 592 (2021) 551–557. https://doi.org/10.1038/s41586-021-03410-9.

[17] H. Wang, X. Wang, M. Li, L. Zheng, D. Guan, X. Huang, J. Xu, J. Yu, Porous Materials Applied in Nonaqueous Li–O2 Batteries: Status and Perspectives, Advanced Materials 32 (2020). https://doi.org/10.1002/adma.202002559.

[18] Z. Gu, X. Xin, J. Yang, D. Guo, S. Yang, J. Wu, Y. Sun, X. Yao, Bilayer NASICON/Polymer Hybrid Electrolyte for Stable Solid-State Li-O2Batteries, ACS Appl Energy Mater 5 (2022) 9149–9157. https://doi.org/10.1021/acsaem.2c01717.

[19] W. Yu, C. Xue, B. Hu, B. Xu, L. Li, C.W. Nan, Oxygen- and dendrite-resistant ultra-dry polymer electrolytes for solid-state Li–O2 batteries, Energy Storage Mater 27 (2020) 244–251. https://doi.org/10.1016/j.ensm.2020.02.001.

[20] Y. Yoon, M.W. Shin, A novel gel polymer electrolyte with multi-functional additive for superior ionic conductivity, stability against Li, and redox activity of lithium-air batteries, Electrochim Acta 462 (2023). https://doi.org/10.1016/j.electacta.2023.142763.

[21] Y. Hou, Z. Chen, R. Zhang, H. Cui, Q. Yang, C. Zhi, Recent advances and interfacial challenges in solid-state electrolytes for rechargeable Li-air batteries, Exploration 3 (2023). https://doi.org/10.1002/exp.20220051.

[22] M. Wang, Y. Yao, F. Yang, Z. Tang, J. Ren, C. Zhang, F. Wu, X. Wang, Double spatial confinement on ruthenium nanoparticles inside carbon frameworks as durable catalysts for a quasi-solid-state Li–O2 battery, Carbon Energy (2023). https://doi.org/10.1002/cey2.334.

[23] N. Feng, C. Wang, J. Wang, Y. Lin, G. Yang, A High-Performance Li-O2/Air Battery System with Dual Redox Mediators in the Hydrophobic Ionic Liquid-Based Gel Polymer Electrolyte, Batteries 9 (2023). https://doi.org/10.3390/batteries9050243.

[24] M. Song, C. Tian, X. Xu, T. Huang, A. Yu, In Situ Thermal Polymerization of a Succinonitrile-Based Gel Polymer Electrolyte for Lithium-Oxygen Batteries, ACS Appl Mater Interfaces 15 (2023) 20159–20165. https://doi.org/10.1021/acsami.3c02155.

[25] M. Sun, X. Sun, Z. Wang, S. Guo, G. Yu, H. Yang, Synthesis and properties of gelatin methacryloyl (GelMA) hydrogels and their recent applications in load-bearing tissue, Polymers (Basel) 10 (2018). https://doi.org/10.3390/POLYM10111290.

[26] G. Ying, N. Jiang, C. Yu, Y.S. Zhang, Three-dimensional bioprinting of gelatin methacryloyl (GelMA), Biodes Manuf 1 (2018) 215–224. https://doi.org/10.1007/s42242-018-0028-8.

[27] P. Chansoria, S. Asif, K. Polkoff, J. Chung, J.A. Piedrahita, R.A. Shirwaiker, Characterizing the Effects of Synergistic Thermal and Photo-Cross-Linking during Biofabrication on the Structural and Functional Properties of Gelatin Methacryloyl (GelMA) Hydrogels, ACS Biomater Sci Eng 7 (2021) 5175–5188. https://doi.org/10.1021/acsbiomaterials.1c00635.

[28] S. Ramesh, M. Ramalingam, Aqueous-mediated synthesis and characterization of gelatin methacryloyl for biomedical applications, Biointerface Res Appl Chem 12 (2022) 6269–6279. https://doi.org/10.33263/BRIAC125.62696279.

[29] J. Yao, M. Hakkarainen, Methacrylated wood flour-reinforced “all-wood” derived resin for digital light processing (DLP) 3D printing, Composites Communications 38 (2023). https://doi.org/10.1016/j.coco.2023.101506.

[30] M. Longo, M. Gandolfo, C. Francia, S. Bodoardo, M. Sangermano, J. Amici, Gelatine based gel polymer electrolyte towards more sustainable Lithium-Oxygen batteries, Electrochim Acta 466 (2023) 143026. https://doi.org/10.1016/j.electacta.2023.143026.

[31] Q. Wu, L. Wang, P. Ding, Y. Deng, O.V. Okoro, A. Shavandi, L. Nie, Mercaptolated chitosan/methacrylate gelatin composite hydrogel for potential wound healing applications, Composites Communications 35 (2022). https://doi.org/10.1016/j.coco.2022.101344.

[32] K. Rahali, G. Ben Messaoud, C.J.F. Kahn, L. Sanchez-Gonzalez, M. Kaci, F. Cleymand, S. Fleutot, M. Linder, S. Desobry, E. Arab-Tehrany, Synthesis and characterization of nanofunctionalized gelatin methacrylate hydrogels, Int J Mol Sci 18 (2017). https://doi.org/10.3390/ijms18122675.

[33] C. Stani, L. Vaccari, E. Mitri, G. Birarda, FTIR investigation of the secondary structure of type I collagen: New insight into the amide III band, Spectrochim Acta A Mol Biomol Spectrosc 229 (2020). https://doi.org/10.1016/j.saa.2019.118006.

[34] T.S. Anirudhan, A.M. Mohan, Novel pH sensitive dual drug loaded-gelatin methacrylate/methacrylic acid hydrogel for the controlled release of antibiotics, Int J Biol Macromol 110 (2018) 167–178. https://doi.org/10.1016/j.ijbiomac.2018.01.220.

[35] C. Li, C. Mu, W. Lin, Novel hemocompatible nanocomposite hydrogels crosslinked with methacrylated gelatin, RSC Adv 6 (2016) 43663–43671. https://doi.org/10.1039/c6ra04609f.

[36] J.L. Pablos, J. Jiménez-Holguín, S.S. Salcedo, A.J. Salinas, T. Corrales, M. Vallet-Regí, New Photocrosslinked 3D Foamed Scaffolds Based on GelMA Copolymers: Potential Application in Bone Tissue Engineering, Gels 9 (2023). https://doi.org/10.3390/gels9050403.

[37] Y. Huang, J. Xu, J. Shao, G. Sun, D. Li, Q. Fan, Blue light induced photopolymerization and cross-linking kinetics of poly(acrylamide) hydrogels, Langmuir 36 (2020) 11676–11684. https://doi.org/10.1021/acs.langmuir.0c02560.

[38] H. S. Yang, M. P. Wolcott, H. S. Kim, H. J. Kim, Thermal Properties of Lignocellulosic Filler-Thermoplastic Polymer Bio-Composites, Journal of Thermal Analysis and Calorimetry 82 (2005) 157-160. https://doi.org/10.1007/s10973-005-0857-5.

[39] K. Dokko, D. Watanabe, Y. Ugata, M.L. Thomas, S. Tsuzuki, W. Shinoda, K. Hashimoto, K. Ueno, Y. Umebayashi, M. Watanabe, Direct Evidence for Li Ion Hopping Conduction in Highly Concentrated Sulfolane-Based Liquid Electrolytes, Journal of Physical Chemistry B 122 (2018) 10736–10745. https://doi.org/10.1021/acs.jpcb.8b09439.

[40] K. Oldiges, D. Diddens, M. Ebrahiminia, J.B. Hooper, I. Cekic-Laskovic, A. Heuer, D. Bedrov, M. Winter, G. Brunklaus, Understanding transport mechanisms in ionic liquid/carbonate solvent electrolyte blends, Physical Chemistry Chemical Physics 20 (2018) 16579–16591. https://doi.org/10.1039/c8cp01485j.

[41] M. Ara, T. Meng, G.-A. Nazri, S.O. Salley, K.Y. Simon Ng, Ternary Imidazolium-Pyrrolidinium-Based Ionic Liquid Electrolytes for Rechargeable Li-O 2 Batteries , J Electrochem Soc 161 (2014) A1969–A1975. https://doi.org/10.1149/2.0031414jes.

[42] R. Naderi, A. Gurung, Z. Zhou, G. Varnekar, K. Chen, J. Zai, X. Qian, Q. Qiao, Activation of Passive Nanofillers in Composite Polymer Electrolyte for Higher Performance Lithium-Ion Batteries, Adv Sustain Syst 1 (2017). https://doi.org/10.1002/adsu.201700043.

[43] H. Zhang, H. Lu, J. Chen, Y. Nuli, J. Wang, A Novel Filler for Gel Polymer Electrolyte with a High Lithium-Ion Transference Number toward Stable Cycling for Lithium-Metal Anodes in Lithium-Sulfur Batteries, ACS Appl Mater Interfaces 13 (2021) 48622–48633. https://doi.org/10.1021/acsami.1c12736.

[44] X. Liu, X. Xin, L. Shen, Z. Gu, J. Wu, X. Yao, Poly(methyl methacrylate)-Based Gel Polymer Electrolyte for High-Performance Solid State Li-O2Battery with Enhanced Cycling Stability, ACS Appl Energy Mater 4 (2021) 3975–3982. https://doi.org/10.1021/acsaem.1c00344.

[45] A. Chamaani, N. Chawla, M. Safa, B. El-Zahab, One-Dimensional Glass Micro-Fillers in Gel Polymer Electrolytes for Li-O2 Battery Applications, Electrochim Acta 235 (2017) 56–63. https://doi.org/10.1016/j.electacta.2017.03.064.

[46] M. Song, C. Tian, T. Huang, A. Yu, Hybrid Ceramic-Gel Polymer Electrolyte with a 3D Cross-Linked Polymer Network for Lithium-Oxygen Batteries, ACS Appl Energy Mater 6 (2023) 7681–7691. https://doi.org/10.1021/acsaem.3c01183.

[47] M. Celik, S. Pakseresht, A.W.M. Al-Ogaili, S. Usta, H. Akbulut, T. Cetinkaya, A Novel Approach for Development of Stable Quasi-Solid Lithium-O2 Batteries: Assembly and Performances of Double Layer Gel Polymer Electrolytes, Batter Supercaps 6 (2023). https://doi.org/10.1002/batt.202300263.

[48] C. Guo, K. Du, R. Tao, Y. Guo, S. Yao, J. Wang, D. Wang, J. Liang, S.Y. Lu, Inorganic Filler Enhanced Formation of Stable Inorganic-Rich Solid Electrolyte Interphase for High Performance Lithium Metal Batteries, Adv Funct Mater 33 (2023). https://doi.org/10.1002/adfm.202301111.

[49] C. Gao, X. Li, G. Wei, S. Wang, X. Zhao, F. Kong, In-situ construction of cellulose acetate propionate-based hybrid gel polymer electrolyte for high-performance lithium metal batteries, Ind Crops Prod 204 (2023). https://doi.org/10.1016/j.indcrop.2023.117395.

[50] Z. Lian, Y. Lu, S. Zhao, Z. Li, Q. Liu, Engineering the Electronic Interaction between Atomically Dispersed Fe and RuO2 Attaining High Catalytic Activity and Durability Catalyst for Li-O2 Battery, Advanced Science 10 (2023). https://doi.org/10.1002/advs.202205975.

[51] Y. Hou, J. Wang, J. Liu, C. Hou, Z. Xiu, Y. Fan, L. Zhao, Y. Zhai, H. Li, J. Zeng, X. Gao, S. Zhou, D. Li, Y. Li, F. Dang, K. Liang, P. Chen, C. Li, D. Zhao, B. Kong, Interfacial Super-Assembled Porous CeO2/C Frameworks Featuring Efficient and Sensitive Decomposing Li2O2 for Smart Li–O2 Batteries, Adv Energy Mater 9 (2019). https://doi.org/10.1002/aenm.201901751.

[52] H. Liu, W. Li, H. Chang, H. Hu, S. Cui, C. Hou, W. Liu, Y. Jin, Micro Area Interface Wetting Structure with Tailored Li+-Solvation and Fast Transport Properties in Composite Polymer Electrolytes for Enhanced Performance in Solid-State Lithium Batteries, ACS Appl Mater Interfaces 16 (2024) 3489–3501. https://doi.org/10.1021/acsami.3c16609.

[53] J.W. Kim, M.K. Oh, Y.A. Kim, U.T. Nakate, E.J. Kwon, S. Seo, W.K. Kim, K.H. Ryu, D.W. Kim, Enhanced cycle life of lithium metal batteries via modulating the lithium-ion solvation sheath with a cross-linked gel polymer electrolyte, J Power Sources 598 (2024). https://doi.org/10.1016/j.jpowsour.2024.234183.

[54] S. Ganapathy, B.D. Adams, G. Stenou, M.S. Anastasaki, K. Goubitz, X.F. Miao, L.F. Nazar, M. Wagemaker, Nature of Li2O2 oxidation in a Li-O2 battery revealed by operando X-ray diffraction, J Am Chem Soc 136 (2014) 16335–16344. https://doi.org/10.1021/ja508794r.

[55] K.P.C. Yao, D.G. Kwabi, R.A. Quinlan, A.N. Mansour, A. Grimaud, Y.-L. Lee, Y.-C. Lu, Y. Shao-Horn, Thermal Stability of Li 2 O 2 and Li 2 O for Li-Air Batteries: In Situ XRD and XPS Studies , J Electrochem Soc 160 (2013) A824–A831. https://doi.org/10.1149/2.069306jes.

[56] H. Lim, E. Yilmaz, H.R. Byon, Real-time XRD studies of Li-O 2 electrochemical reaction in nonaqueous lithium-oxygen battery, Journal of Physical Chemistry Letters 3 (2012) 3210–3215. https://doi.org/10.1021/jz301453t.

[57] F. Tian, M.D. Radin, D.J. Siegel, Enhanced charge transport in amorphous Li2O2, Chemistry of Materials 26 (2014) 2952–2959. https://doi.org/10.1021/cm5007372.

[58] Y. Zhang, Q. Cui, X. Zhang, W.C. McKee, Y. Xu, S. Ling, H. Li, G. Zhong, Y. Yang, Z. Peng, Amorphous Li2O2: Chemical Synthesis and Electrochemical Properties, Angewandte Chemie - International Edition 55 (2016) 10717–10721. https://doi.org/10.1002/anie.201605228.

[59] Y. Li, R. Zhang, B. Chen, N. Wang, J. Sha, L. Ma, D. Zhao, E. Liu, S. Zhu, C. Shi, N. Zhao, Induced construction of large-area amorphous Li2O2 film via elemental co-doping and spatial

confinement to achieve high-performance Li-O2 batteries, Energy Storage Mater 44 (2022) 285–295. https://doi.org/10.1016/j.ensm.2021.10.026.

[60] J. Wang, L. Ma, J. Xu, Y. Xu, K. Sun, Z. Peng, Oxygen electrochemistry in Li-O 2 batteries probed by in situ surface-enhanced Raman spectroscopy , SusMat 1 (2021) 345–358. https://doi.org/10.1002/sus2.24.

[61] H. Kim, K.J. Min, M.G. Jeong, H.G. Jung, Y.K. Sun, Resolving the Incomplete Charging Behavior of Redox-Mediated Li-O2Batteries via Sustainable Protection of Li Metal Anode, ACS Appl Mater Interfaces 14 (2022) 45945–45953. https://doi.org/10.1021/acsami.2c14349.